RSC Advances

ROYAL SOCIETY OF CHEMISTRY

www.rsc.org/advances

Journal Name

RSCPublishing

ARTICLE

Formation Kinetics and Photoelectrochemical Properties of Crystalline C_{70} One-Dimensional Microstructures

Cite this: DOI: 10.1039/x0xx00000x

Shushu Zheng and Xing Lu*

Received 00th January 2012,
Accepted 00th January 2012

DOI: 10.1039/x0xx00000x

www.rsc.org/

Assembling the sub-nanometer fullerene molecules into ordered microstructures is a necessary step towards their applications but concise morphology control of the ordered structures is very challenging and the formation mechanism is still a big mystery. We herein report the preparation and morphology control of different C_{70} one-dimensional (1D) microstructures using regioisomers of xylenes as good solvents and isopropyl alcohol (IPA) as the poor solvent by the interfacial precipitation method. Our systematic investigations show that the solvents participating in the formation process of these C_{70} 1D microstructures play a critical role in determining the morphology, crystalline structure, formation process and intrinsic properties of these materials. Furthermore, we have also investigated the photoelectrochemical properties of these C_{70} 1D microstructures, proving their potential applications in related fields.

1. Introduction

Carbon nanomaterials of unique structures have received considerable attention during recent years. Typical examples are the zero-dimensional (0D) fullerene, the one-dimensional (1D) carbon nanotube, and the two-dimensional (2D) graphene.[1-3] Among them, fullerenes are particularly unique because of their definitive molecular structures and high solubility in organic solvents.[4] Assembly of the sub-nanometer fullerene molecules into nano/microstructures is a practical way to realize their ultimate applications in various fields.[5-8] Among the various methods for the preparation of fullerene nano/microstructures,[9-15] the interfacial precipitation method using mixture solvents consisted of a good solvent and an antisolvent shows high potential in the morphology control of fullerene crystals because of its facileness and versatility.[8, 16-20] Compared to various C_{60} crystals obtained by the this method,[16-23] geometrically well-defined C_{70} crystals[7, 24-26] are less-studied and concise control of the morphologies of C_{70} nano/microstructures is still a big challenge. Moreover, although it is widely acknowledged that the solvents play a crucial role in the morphology control or crystalline determination of the fullerene crystals, and thus subtle variation of the solvent types[17, 21, 22, 27] or solvent ratios[7, 16, 17, 20, 28] can remarkably change the morphological features of the products, it is still unclear how the solvents participate in the formation process during the precipitation.

Herein, to gain an in-depth understanding of solvent effect on the C_{70}-crystal formation during the precipitation process, we conducted a systematical study by employing three regioisomers of xylenes as the good solvents and isopropyl alcohol (IPA) as the antisolvent to get various C_{70} nano/microstructures with different morphological features. It is revealed for the first time that the content of solvent-doping in the formed crystals is a critical factor in controlling the morphologies and formation kinetics of these C_{70} microstructures. A kinetically favored process is observed for C_{70}/*m*-xylene/IPA system, which results in nanometer-sized cylindrical nanorods with a high content of solvent (9.45%). In contrast, the microstructures obtained from either the C_{70}/*p*-xylene/IPA or the C_{70}/*o*-xylene/IPA system are large hexagonal prisms with relatively low solvent-contents, confirming that the formation mechanisms are both thermodynamic processes. Finally, it is demonstrated that these well-ordered C_{70} 1D microstructures exhibit excellent photoconductive properties with spectral responses covering ultraviolet to visible region, illuminating their future applications as optical sensors. Our results have shed new light on the morphology control, formation mechanism and application of the less studied C_{70} nano/microstructures, which will stimulate broad interests from across multidisciplinary fields.

2. Experimental Section

Preparation of C_{70} 1D Microstructures

O-xylene, *m*-xylene and *p*-xylene were employed as the respective good solvent of C_{70} and IPA as the poor solvent in all cases. The concentration of C_{70} in *p*-xylene or *m*-xylene was set to be 2 mg/mL, but the concentration in *o*-xylene was 4 mg/mL because a lower concentration of C_{70} (e.g. 2 mg/mL) in *o*-xylene did not trigger any precipitate under the same conditions. Typically, 5 mL C_{70} solution was rapidly injected into 10 mL IPA to form a turbid solution instantly. Then the solution was aged for 12 h to precipitate. The suspension was separated by centrifugation and was washed with IPA for several times. The samples freshly obtained from the mixed solvents without any heat treatment are designated as C70-O, C70-M, C70-P when *o*-xylene, *m*-xylene, *p*-xylene are used as solvents, respectively. The samples were further treated with vacuum drying at 60 °C over-night to remove the solvents absorbed on the surface. These samples are defined as C70-O-60 (solvent: *o*-xylene, 60 °C vacuum drying), C70-M-60 (solvent: *m*-xylene, 60 °C vacuum drying) and C70-P-60 (solvent: *p*-xylene, 60 °C vacuum drying). Then the obtained solid samples were also annealed at 150 °C for 5 h in N_2 atmosphere to ensure the complete elimination of any

intercalated solvents in the C_{70} crystals. This leads to the finding of the phase-transformation process of the nanostructures obtained from *m*-xylene/IPA system (vide infra). These samples are labeled as follows: C70-O-150 (solvent: *o*-xylene, 150 °C annealing in N_2), C70-M-150 (solvent: *m*-xylene, 150 °C annealing in N_2), C70-P-150 (solvent: *p*-xylene, 150 °C annealing in N_2).

Characterizations

SEM images were collected with either a Nova NanoSEM 450 or a JEOL 6701F electron microscopy operating at an accelerating voltage of 10 kV. Transmission electron microscope (FEI Tecnai G2 T20 or F30) was applied to obtain transmission electron microscopy (TEM) images, high-resolution transmission electron microscopy (HRTEM) images and selected area electron diffraction (SAED) patterns. All the X-ray diffraction measurements were carried out with Empyrean diffractometer with Cu Kα radiation (λ = 0.1541 nm, operated at 40 kV and 40 mA). The composition of the sample was confirmed by FT-IR (Brucker Tensor-27 FT-IR) and Raman spectra (Bruker VERTEX 70). Thermo-gravimetric analysis (TGA, Diamond TG/DTA) was performed to determine the solvent content in the sample. UV-vis spectra were obtained from a Lambda 750S spectrometer.

Photocurrent measurements

The photocurrent tests were carried out in a three-electrode system consisting of a working electrode (C_{70} microstructure film), an Ag/AgCl reference electrode and a platinum wire counter electrode, by using a CHI 660E electrochemical workstation at room temperature and a 500 W xenon lamp (Saifan Photoelectronic Co., 7IPX5002) as light source. The electrolyte was 0.1 M KCl aqueous solution. The work electrode was made as follows: indium tin oxide (ITO) was used as current collector and IPA dispersions of the corresponding C_{70} microstructures were deposited onto ITO by drop-casting. Two filters were used to obtain the visible light source (400 - 800 nm) and UV light source (350 nm). All photoelectrochemical experiments were carried out under Ar atmosphere.

3. Results and discussion

Morphological Characterizations

The SEM and TEM images of the as-prepared C_{70} microstructures are shown in Fig. 1. Although all these microstructures display one-dimensional morphological appearances, their detailed structures and diameters/lengths are totally different from each other. C70-O and C70-P both exhibit hexagonal cross-sections with pyramidal ends but C70-P displays an appearance with two tube-like ends and a solid center (Fig. 1c3) which we assume may be a consequence of concentration depletion.[20]. In contrast, C70-M nanostructures display cylindrical solid shapes. As summarized in Table 1 and Fig. S1, C70-O hexagonal microrods are 1.9 - 3.5 μm wide and 19.0 - 31.0 μm long with a statistic diameter of 2.7 μm and a mean length of 26.0 μm. Similarly, the widths of C70-P microtubes range from 1.9 to 3.3 μm, and the lengths fall into the range of 19.0 - 31.0 μm. The statistic diameter and length of C70-P microtubes are 2.5 μm and 23.9 μm, respectively. In sharp contrast, the C70-M nanorods are thinner and shorter with a narrow diameter distribution of 0.35 - 0.75 μm and a narrow length range of 5.0 - 11.0 μm, and the mean diameter is 0.47 μm and the mean length is 9.8 μm. The morphological differences of these microstructures must be caused by the different solvents used in the experiments because other experimental conditions are identical.

Crystalline Configuration and Composition

X-ray diffraction (XRD) measurements are effective to investigate the crystalline structures of organic and inorganic materials. The powder XRD patterns of these C_{70} 1D microstructures obtained from 60 °C vacuum drying are shown in Fig. 2a. It is clear that C70-P-60 and C70-O-60 display similar XRD patterns to that of C_{70} powder, which are indexed as (001), (002), (101), (102), (110), (103), (112) diffraction peaks, corresponding to an hcp lattice.[29] In contrast, C70-M-60 has an orthorhombic lattice, indexed as (002), (011), (102), (004), (024), (213) and (008) diffraction peaks, which is similar to that of the toluene-solvated phase reported previously.[30] The XRD patterns of untreated samples freshly obtained from mixed solvents are shown in Fig. S2, which are same to those of the corresponding samples treated at 60 °C. However, after annealing at 150 °C,

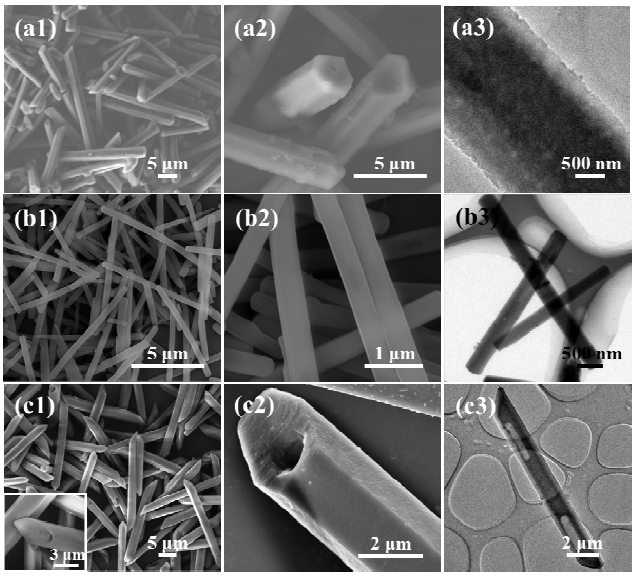

Fig. 1 SEM images (a1-c1, a2-c2) and TEM images (a3-c3) of C_{70} 1D microstructures prepared from different solvents. (a) C70-O, (b) C70-M and (c) C70-P.

Table 1 Size distributions of C_{70} 1D microstructures obtained from different solvents.

Sample number	C70-O	C70-M	C70-P
Diameter (μm)	1.9 - 3.5	0.35 - 0.75	1.9 - 3.3
Length (μm)	19.0 - 31.0	5.0 - 11.0	19.0 - 31.0

C70-M-150 shows a XRD pattern of the fcc phase (Fig. 2b), although C70-O-150 and C70-P-150 still retain the hcp structures. The unit cell dimensions of these samples determined by XRD measurements are listed in Table 2. The orthorhombic C70-M-60 crystals have the unit cell dimensions of a = 10.49 Å, b = 11.14 Å, c = 35.05 Å.[31] After annealing at 150 °C, the orthorhombic structure evolves to the fcc structure with lattice constants of $a = b = c$ = 14.87 Å.[31] The space lattices of C70-O-60 and C70-P-60 both correspond to the hcp structure (c/a = 1.63),[31] with the unit cell dimensions of $a = b$ = 11.15 Å, c = 17.91 Å for C70-O-60 and $a = b$ = 11.10 Å, c = 17.70 Å for C70-P-60, respectively (Table 2). They are slightly

different from each other due to the incorporation of different solvent molecules. After annealing at 150 °C for 5 h, the crystalline types are not changed, but the unit cell dimensions slightly differ from the corresponding precursors, with $a = b = 11.02$ Å, $c = 17.99$ Å for C70-O-150 and $a = b = 10.99$ Å, $c = 17.90$ Å for C70-P-150 (Table 2), most probably due to the loss of the solvent molecules from the crystal cavities.

In situ variable temperature X-ray diffraction (VT-XRD) measurements were carried out to further examine the crystalline transformation processes of these C_{70} 1D microstructures. As illustrated in Fig. 2d, a conspicuous transformation of XRD patterns between 100 and 150 °C is observed for C70-M-60. This temperature range is consistent with the boiling point of *m*-xylene

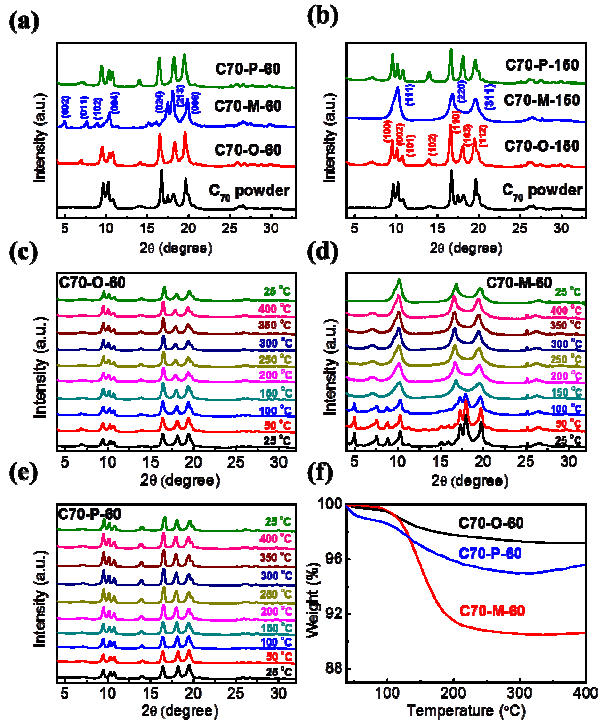

Fig. 2 XRD patterns of C_{70} powder and as-prepared C_{70} 1D microstructures (a) after vacuum drying at 60 °C and (b) after annealing at 150 °C for 5 h; *In situ* VT-XRD patterns of (c) C70-O-60, (d) C70-M-60, (e) C70-P-60 in the temperature range between 25 °C and 400 °C.

(139 °C). Accordingly, we speculate that this crystalline phase transformation is caused by the loss of the solvent molecules trapped in the crystal lattice. Although previous studies reported that the evaporation of the trapped solvents in C_{60} crystals is fast even at room temperature or under vacuum,[32, 33] our results demonstrate that the elimination of the solvents in these C_{70} crystals is rather difficult which requires a higher temperature. We assume here that the ellipsoidal C_{70} molecules are more suitable to prevent the escape of solvent molecules from the closely packed crystal lattice. In comparison, the VT-XRD results of C70-O-60 and C70-P-60 (Fig. 2c and 2e) demonstrate that the hcp structures remain unchanged at high temperatures, because it is almost as stable as the closely packed fcc phase of C_{70}.[31] A significant mass loss (9.45%) of C70-M-60 between 80 and 200 °C is observed in the TGA results (Fig. 2f) but much smaller values are obtained for C70-O-60 and C70-P-60 (2.68% and 3.64%, respectively). Consistently, the FTIR spectrum of C70-M-60 (Fig. S3a) shows a clear solvent peak at 766.5 cm^{-1} ascribing to the trapped *m*-xylene molecules,[19, 27, 34] but no obvious absorption peaks of solvents in the samples of C70-O-60 and C70-P-60 are observed because of the low content of the trapped solvents in the lattice cavities. The much higher corporation of *m*-xylene in C_{70} crystals compared to that of *o*-xylene or *p*-xylene can be explained by geometrical differences, similar to the cases of C_{60} crystals.[27] Combining the above results, we speculate that the formation of C70-M nanostructures should be a kinetic process whereas the formation processes of C70-O and C70-P micro-structures are both thermodynamically favourable. It appears that a high content of solvent-doping in the crystalline structures results in relatively small cylindrical nanorods and a low content of solvents tends to give large microstructures with hexagonal cross-sections (Table 1).

Morphology Elucidation of C70-P Hexagonal Microstructures

Both C70-O and C70-P exhibit hexagonal cross-sections which arouse our interests to perform lattice-resolved HRTEM studies of their internal structures. The TEM results of C70-P are shown in Fig. 3 as a representative and those of C70-O are put in Fig. S4. From Fig. 3a, the interplanar spacing values of 0.54 and 0.88 nm can be easily attributed to the lattice constants of (110) and (002) plane, respectively, showing the preferential growth along the [001] direction (Fig. 3b). Considering the hexagonal prism structures, we conclude that the (100), (110) and (010) planes form the hexagonal prism (Fig. 3c). The angle between the longitudinal rod axis and the intersecting line of two pyramidal planes is 36.1 ° (Fig. S5), which leads to the assignment of the lattice planes of the pyramidal tip to be $(10\bar{1})$, $(11\bar{1})$, (011) and (111) planes (Fig. 3c). A schematic model of a microtube of C70-P is drawn in Fig. 3c. The formation of the prism-shaped C_{70} crystals is attributed to the difference in the growth rate of the crystal facets.[35] In present study, the disappearance of the (001) plane may result from the fairly rapid growth rate along this plane. Therefore, the {111} planes forms the pyramidal tips at the end of *c*-axis, while the {110} planes remains to form hexagonal prisms. Since the case of C70-O is similar to that of C70-P where the growth axis is also the [001] direction (Fig. S4b), the schematic model for C70-P is also suitable to interpret the internal structure of C70-O.

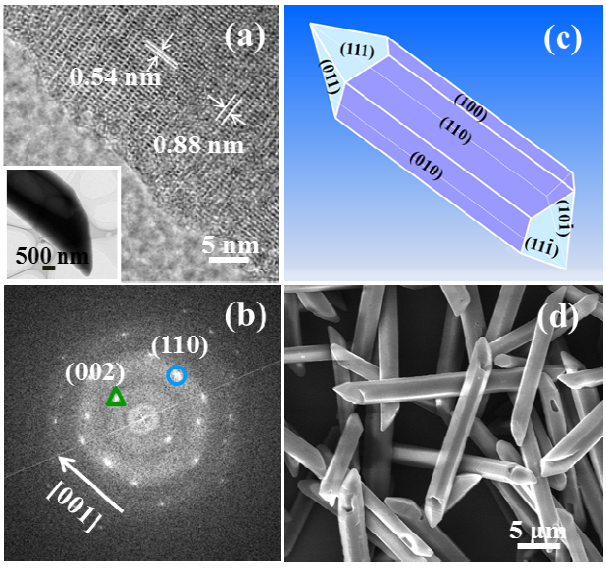

Fig. 3 (a) HRTEM and (b) fast Fourier transform (FFT) image of a microtube of C70-P which is shown in the inset of (a); (c) A

schematic model for a hexagonal microtube of C70-P; (d) SEM image of C70-P microtubes.

Phase Transformation Model for C70-M

HRTEM measurements were also conducted to clarify the phase transformation process from C70-M-60 (orthorhombic) to C70-M-150 (fcc). Fig. 4 displays the corresponding HRTEM images and SAED patterns, proving that both are single crystals. Combining the XRD, TGA and TEM results together, we propose an interpretation model for the phase transformation from the orthorhombic lattice to the fcc lattice for C70-M nanorods (Scheme 1).[30] From the TGA result, the molar ratio of C_{70} to *m*-xylene in C70-M-60 is calculated to be 5:4. Thus, the initial orthorhombic unit cell is formed by five C_{70} molecules inside which four *m*-xylene molecules are trapped ($5C_{70}{\cdot}4m$-xylene) (Scheme 1a). Under higher temperatures, however, the solvents evaporate from the crystal lattice and the bct structure (defined in the fcc cell, Scheme 1b) is formed by the shrinkage of the *c*-axis of the orthorhombic cell along with an alternate shearing displacement along the *b*-axis (Scheme 1d).

This model (Scheme 1) is also consistent with the HRTEM results (Fig. 4). For C70-M-60, the lattice spacing along the longitudinal rod axis is 0.52 nm, corresponding to the (200) plane. The parallel crystal spacing is 1.15 nm which corresponds to the (011) plane. For C70-M-150, the discrete diffraction spots in Fig. 4d are indexed according to the fcc structure, in which the *d*(220) lattice spacing is also 0.52 nm, and the [110] direction is parallel to the longitudinal rod axis. As shown in Fig. 4a and 4c, the (100) plane of the orthorhombic cell (*d*-spacing: 1.04 nm) and the (110) plane of the fcc cell (*d*-spacing: 1.04 nm) are both perpendicular to the longitudinal axis of the C_{70} rods, and the *d*-spacing values of these two planes are identical. This confirms that the (100) plane of the orthorhombic cell is superposed with the (110) plane of the fcc cell, as clearly shown in Scheme 1.

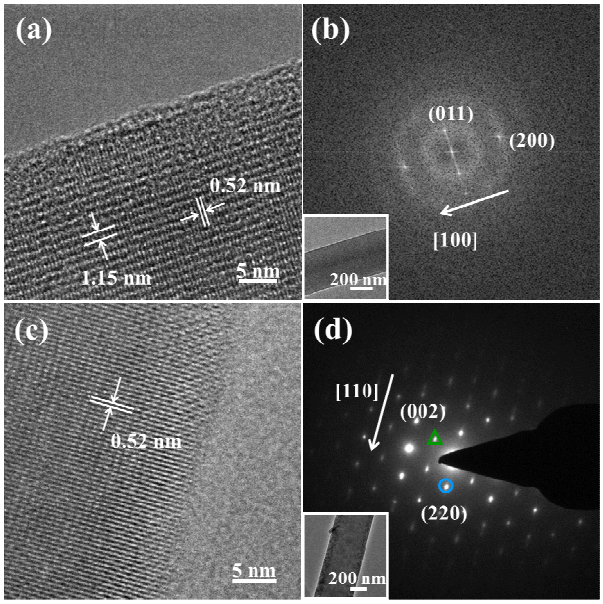

Fig. 4 (a) HRTEM and (b) FFT images of a C70-M-60 nanorod which is shown in the inset of (b). (c) HRTEM image and (d) SAED pattern of a C70-M-150 nanorod which is shown in the inset of (d).

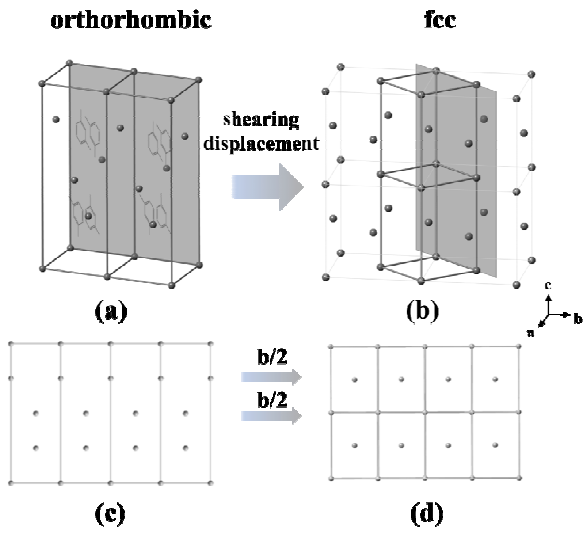

Scheme 1 Schematic illustration showing phase transformation from the orthorhombic phase of C70-M-60 to the fcc phase of C70-M-150. (a) The pristine orthorhombic unit cell of $5C_{70}{\cdot}4m$-xylene. (b) The fcc unit cell obtained after transformation (light lines) in which the bct cell is defined with bold bonds. (c) Projection from *a*-axis of the original orthorhombic cell. (d) Projection from the $[1\ \bar{1}\ 0]$ direction of the bct cell. The shrinkage in the *c*-axis and the alternate shearing displacement along the b-axis after solvent-loss cause a transformation to the bct unit cell. The shaded portion in (a) represents the (100) plane of the orthorhombic cell and that in (b) represents the (110) plane of the fcc cell. The grey dots represent C_{70} molecules.

Growth Mechanism

To gain more information about the formation processes of these C_{70} 1D microstructures, we collected the SEM images of the samples at different time scales after the injection of the corresponding C_{70} solutions into IPA. The morphology evolution processes of these C_{70} 1D microstructures are shown in Fig. 5 and the plausible growth mechanisms are illustrated in Scheme 2. It is evident that C_{70} clusters

Table 2 Crystalline types and unit cell dimensions of C_{70} 1D microstructures under study.

Sample	C70-O-60	C70-O-150	C70-M-60	C70-M-150	C70-P-60	C70-P-150
Crystalline type	hcp	hcp	orthorhombic	fcc	hcp	hcp
a (Å)	11.15	11.02	10.49	14.87	11.10	10.99

b (Å)	11.15	11.02	11.14	14.87	11.10	10.99
c (Å)	17.91	17.99	35.05	14.87	17.70	17.90

nucleate instantly after the injection. As the case for C_{70}/*o*-xylene/IPA, C_{70} nanorod-bundles are formed initially,[36] and then they grow longer and fuse together to form the final hexagonal microrods. However, the case of C_{70}/*m*-xylene/IPA is markedly different. In the beginning, C_{70} crystals grow in various directions to form the large star-like crystals that subsequently disconnect to generate the microrods along with the depletion of C_{70} nuclei. Finally, the microrods branch to form smaller rods (inset of Fig. 5b2) which eventually afford the individual nanorods after the matrix microrods are depleted. For the C_{70}/*p*-xylene/IPA system, preliminary hexagonal nuclei (Fig. 5c1) are formed instead of hierarchical structures consisting of cylindrical nanorods (Fig. 5a1 and 5b1). Then the hexagonal nuclei grow in two opposite directions to form the final hexagonal microtubes with two hollow ends. To conclude, C_{70} crystals obtained from the C_{70}/*o*-xylene/IPA or C_{70}/*p*-xylene/IPA are formed by unidirectional growth of the initial nuclei. In contrast, for C_{70}/*m*-xylene/IPA, the C_{70} crystals tend to grow along multi-directions. This is a clear indication of the kinetically driven growth process which results in smaller nanorods without preferentially exposed facets but with a high content of solvent molecules. In contrast, both the growth processes of C70-O and C70-P are thermodynamically favoured, which afford large equilibrium microstructures with preferred hexagonal prism appearances.

In conclusion, we confirmed unambiguously that the intercalation of solvent molecules into the crystal lattice affects the molecular arrangement of the crystalline structures and determines the kinetic pathways toward aggregation.[37, 38] In particular, the formation of the nanorods for C_{70}/*m*-xylene/IPA is a kinetically driven process so that the initially formed orthorhombic structure evolves to the thermodynamically more stable fcc structure under heating. This is a clear observation of the solvent effect on the growth pattern of fullerene nano/microstructures.

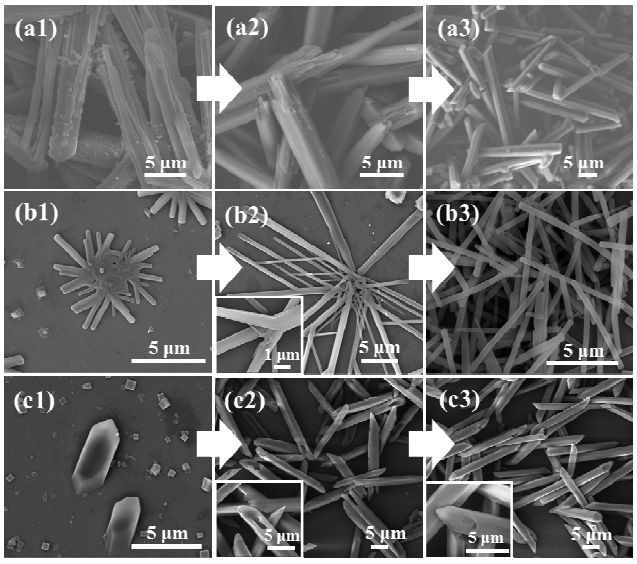

Fig. 5 Mechanism studies of the corresponding C_{70} microcrystals of different time scales in different solvent systems with SEM. (a) C_{70}/*o*-xylene/IPA, (b) C_{70}/*m*-xylene/IPA, (c) C_{70}/*p*-xylene/IPA. (a1, b1, c1) samples obtained as soon as the corresponding C_{70} solutions were added into IPA. (a2, b2, c2) samples obtained after 10 min growth. (a3, b3, c3) samples obtained after 1 h growth.

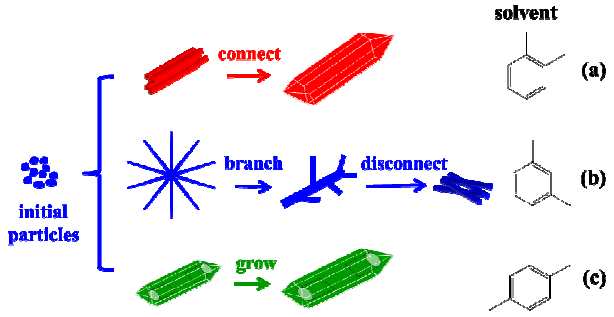

Scheme 2 Schematic illustration of the formation processes of C_{70} 1D microstructures from different solvent interfaces, (a), (b) and (c) represent for C_{70}/*o*-xylene/IPA, C_{70}/*m*-xylene/IPA and C_{70}/*p*-xylene/IPA, respectively. The dashed lines in (c) correspond to the tube-like structures.

Photoelectrochemical Properties

Carbon-based materials with π-conjugated systems show excellent performances in various fields.[39-41] In this work, the photoelectrochemical properties of C_{70} 1D microstructures are studied. Taking into consideration of the crystalline difference, we examine the electrochemical properties of C70-M-60 (orthorhombic), C70-M-150 (fcc) and C70-P-150 (hcp). As shown in Fig. 6, they all show fast and uniform cathodic photocurrents responding to each on-off event both in visible and ultraviolet (UV) region, indicating p-type photoresponse processes. In contrast, the C_{60} films generally display anodic photocurrents, corresponding to an n-type photoresponse.[42] From the UV-vis absorption spectra (Fig. S6), it is evident that C_{70} microstructures show much broader absorptions in visible region than that of C_{70} solution (Fig. S6b). This phenomenon can be caused by strong intermolecular π-π interactions upon the formation of these ordered microstructures.[28]

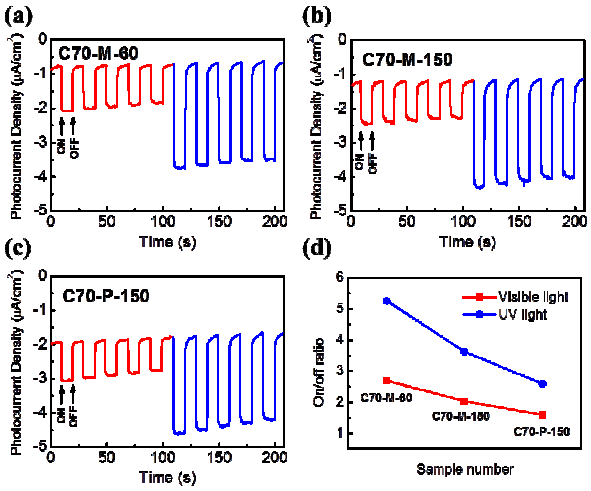

Fig. 6 Photocurrent responses of C_{70} microstructures under visible (400 - 800 nm, red) and UV light (350 nm, blue) irradiation. Condition: 0.1 M KCl aqueous solution at 1 V bias voltage. (a) C70-M-60, (b) C70-M-150, (c) C70-P-150. (d) On/off ratios for different samples under visible light and UV light.

Furthermore, it should be noted that C70-P-150 has the largest dark current and photocurrent both under visible and UV light illumination, while C70-M-60 possesses the smallest values (Fig. 6a-c). However, Fig. 6d clearly shows that C70-M-60 (orthorhombic) has the highest on/off ratio both under visible and UV light illumination. We propose that this phenomenon should be a consequence of the phase differences associated tightly with the incorporation of solvent molecules. The results promise their potential applications as optical sensors.

4. Conclusions

In summary, we have successfully synthesized various 1D microstructures of C_{70} using three different xylene isomers (*o*-xylene, *m*-xylene, *p*-xylene) as the good solvents and isopropyl alcohol as the antisolvent by the precipitation method. The morphology of the as-prepared sample can be readily controlled by changing the solvent. Morphology and mechanism studies reveal that for C_{70}/*o*-xylene/IPA or C_{70}/*p*-xylene/IPA, the nuclei grow in a unidirectional manner to form the final hexagonal microstructures with a low content of solvent participation, which are governed by thermodynamic factor. However, the formation of the nanorods in the *m*-xylene/IPA system is a kinetically favored process which has a multidirectional growth feature resulting in cylindrical nanorods with a high content of solvent molecules. Our results confirm that the solvents play a crucial role in controlling the morphology, the crystalline configuration, the stability and somehow the intrinsic properties of the C_{70} 1D microstructures. Finally, we reveal that these 1D C_{70} microstructures show fast and uniform cathodic photocurrent responses under both visible and UV light irradiation. The present study opens a wide prospect to the morphology control and formation mechanism of C_{70} nano/microstructures, which will fundamentally promote their future applications in related fields.

Acknowledgements

Financial support from The National Thousand Talents Program of China, NSFC (21171061, 51472095), Program for Changjiang Scholars and Innovative Research Team in University (IRT1014) and HUST is gratefully acknowledged. We thank the Analytical and Testing Center in Huazhong University of Science and Technology for related measurements.

Notes and references

State Key Laboratory of Materials Processing and Die & Mould Technology, School of Materials Science and Engineering, Huazhong University of Science and Technology (HUST), Wuhan 430074, P. R. China. E-mail: lux@hust.edu.cn.

† Electronic Supplementary Information (ESI) available: XRD, FTIR and Raman spectra, TEM and SEM images, SAED pattern, and UV-vis absorption spectra of C_{70} 1D microstructures. See DOI: 10.1039/b000000x/

1. W. Kratschmer, L. D. Lamb, K. Fostiropoulos and D. R. Huffman, *Nature*, 1990, **347**, 354-358.
2. S. Iijima, *Nature*, 1991, **354**, 56-58.
3. K. S. Novoselov, A. K. Geim, S. V. Morozov, D. Jiang, Y. Zhang, S. V. Dubonos, I. V. Grigorieva and A. A. Firsov, *Science*, 2004, **306**, 666-669.
4. K. N. Semenov, N. A. Charykov, V. A. Keskinov, A. K. Piartman, A. A. Blokhin and A. A. Kopyrin, *J. Chem. Eng. Data*, 2009, **55**, 13-36.
5. L. K. Shrestha, Q. Ji, T. Mori, K. i. Miyazawa, Y. Yamauchi, J. P. Hill and K. Ariga, *Chem.Asian J.*, 2013, **8**, 1662-1679.
6. H. Li, B. C. K. Tee, J. J. Cha, Y. Cui, J. W. Chung, S. Y. Lee and Z. Bao, *J. Am. Chem. Soc.*, 2012, **134**, 2760-2765.
7. C. Park, E. Yoon, M. Kawano, T. Joo and H. C. Choi, *Angew. Chem. Int. Ed.*, 2010, **49**, 9670-9675.
8. L. Wei, J. Yao and H. Fu, *ACS Nano*, 2013, **7**, 7573-7582.
9. S. I. Cha, K. i. Miyazawa and J.-D. Kim, *Chem. Mater.*, 2008, **20**, 1667-1669.
10. C. Park, H. J. Song and H. C. Choi, *Chem. Commun.*, 2009, 4803-4805.
11. K. Miyazawa, Y. Kuwasaki, A. Obayashi and M. Kuwabara, *J. Mater. Res.*, 2002, **17**, 83-88.
12. S. S. Babu, H. Mohwald and T. Nakanishi, *Chem. Soc. Rev.*, 2010, **39**, 4021-4035.
13. J. Kim, C. Park, J. E. Park, K. Chu and H. C. Choi, *ACS Nano*, 2013, **7**, 9122-9128.
14. S. J. Ahn, J. Yang, K. W. Lim and H. S. Shin, *J. Cryst. Growth*, 2013, **363**, 141-144.
15. B. Wang, X. Gao and G. Piao, *J. Nanomater.*, 2013, **2013**, 5.
16. M. Sathish and K. i. Miyazawa, *J. Am. Chem. Soc.*, 2007, **129**, 13816-13817.
17. J. Jeong, W.-S. Kim, S.-I. Park, T.-S. Yoon and B. H. Chung, *J. Phys. Chem. C*, 2010, **114**, 12976-12981.
18. L. K. Shrestha, J. P. Hill, T. Tsuruoka, K. i. Miyazawa and K. Ariga, *Langmuir*, 2012, **29**, 7195-7202.
19. H.-X. Ji, J.-S. Hu, L.-J. Wan, Q.-X. Tang and W.-P. Hu, *J. Mater. Chem.*, 2008, **18**, 328-332.
20. H.-X. Ji, J.-S. Hu, Q.-X. Tang, W.-G. Song, C.-R. Wang, W.-P. Hu, L.-J. Wan and S.-T. Lee, *J. Phys. Chem. C*, 2007, **111**, 10498-10502.
21. L. K. Shrestha, Y. Yamauchi, J. P. Hill, K. i. Miyazawa and K. Ariga, *J. Am. Chem. Soc.*, 2012, **135**, 586-589.
22. M. Sathish, K. i. Miyazawa, J. P. Hill and K. Ariga, *J. Am. Chem. Soc.*, 2009, **131**, 6372-6373.
23. M. Sathish, K. Miyazawa and T. Sasaki, *Chem. Mater.*, 2007, **19**, 2398-2400.
24. D. Liu, M. Yao, L. Wang, Q. Li, W. Cui, B. Liu, R. Liu, B. Zou, T. Cui, B. Liu, J. Liu, B. Sundqvist and T. Wågberg, *J. Phys. Chem. C*, 2011, **115**, 8918-8922.
25. K. i. Miyazawa, *J. Am. Ceram. Soc.*, 2002, **85**, 1297-1299.
26. D. Liu, W. Cui, N. Yu, R. Liu, D. Liu, Y. Xu, C. Quan, B. Liu, Q. Li and B. Liu, *Cryst. Eng. Comm.*, 2014, **16**, 3284-3288.
27. M. Rana, R. B. Reddy, B. B. Rath and U. K. Gautam, *Angew. Chem. Int. Ed.*, 2014, 1-6.
28. Y. Xu, J. Guo, T. Wei, X. Chen, Q. Yang and S. Yang, *Nanoscale*, 2013, **5**, 1993-2001.
29. M. C. Valsakumar, N. Subramanian, M. Yousuf, P. Sahu, Y. Hariharan, A. Bharathi, V. Sankara Sastry, J. Janaki, G. V. N. Rao, T. S. Radhakrishnan and C. S. Sundar, *Pramana*, 1993, **40**, L137-L144.
30. Y. Takahashi, *Chem. Phys. Lett.*, 1998, **292**, 547-553.
31. A. P. Isakina, A. I. Prokhvatilov, M. A. Strzhemechny and K. A. Yagotintsev, *Low Temp. Phys.*, 2001, **27**, 1037-1047.
32. J.-i. Minato and K. i. Miyazawa, *Carbon*, 2005, **43**, 2837-2841.
33. L. Wang, B. Liu, D. Liu, M. Yao, Y. Hou, S. Yu, T. Cui, D. Li, G. Zou, A. Iwasiewicz and B. Sundqvist, *Adv. Mater.*, 2006, **18**, 1883-1888.
34. L. Wang, B. Liu, S. Yu, M. Yao, D. Liu, Y. Hou, T. Cui, G. Zou, B. Sundqvist, H. You, D. Zhang and D. Ma, *Chem. Mater.*, 2006, **18**, 4190-4194.
35. D. Wang and C. Song, *J. Phys. Chem. B*, 2005, **109**, 12697-12700.
36. Y. Qu, W. Yu, S. Liang, S. Li, J. Zhao and G. Piao, *J. Nanomater.*, 2011, **2011**, 5.
37. P. A. Korevaar, C. Schaefer, T. F. A. de Greef and E. W. Meijer, *J. Am. Chem. Soc.*, 2012, **134**, 13482-13491.
38. C. Park, J. E. Park and H. C. Choi, *Acc. Chem. Res.*, 2014. **47**, 2353-2364.
39. D. Chen, H. Zhang, Y. Liu and J. Li, *Energy Environ. Sci.*, 2013, **6**,

1362-1387.
40. H. Y. Mao, S. Laurent, W. Chen, O. Akhavan, M. Imani, A. A. Ashkarran and M. Mahmoudi, *Chem. Rev.*, 2013, **113**, 3407-3424.
41. D. Chen, H. Feng and J. Li, *Chem. Rev.*, 2012, **112**, 6027-6053.
42. E. S. Shibu, A. Sonoda, Z. Tao, Q. Feng, A. Furube, S. Masuo, L. Wang, N. Tamai, M. Ishikawa and V. Biju, *ACS Nano*, 2012, **6**, 1601-1608.

TOC